Journal of Applied Mathematics and Physics, 2024, 12, 1401-1425
https://www.scirp.org/journal/jamp
ISSN Online: 2327-4379
ISSN Print: 2327-4352

Heat and Mass Transfer for a Nanofluid Flow in Fluidized Bed Dryer in Presence of Induced Magnetic Field

Kiptum J. Purity[1*], Mathew N. Kinyanjui[2], Edward R. Onyango[2]

[1]Pan African University Institute for Basic Sciences, Technology and Innovation, Nairobi, Kenya
[2]Department of Pure and Applied Mathematics, Jomo Kenyatta University of Agriculture and Technology, Nairobi, Kenya
Email: *pkiptum@gmail.com

How to cite this paper: Purity, K.J., Kinyanjui, M.N. and Onyango, E.R. (2024) Heat and Mass Transfer for a Nanofluid Flow in Fluidized Bed Dryer in Presence of Induced Magnetic Field. *Journal of Applied Mathematics and Physics*, **12**, 1401-1425.
https://doi.org/10.4236/jamp.2024.124086

Received: November 19, 2023
Accepted: April 27, 2024
Published: April 30, 2024

Abstract

This research entails the study of heat and mass transfer of nanofluid flow in a fluidized bed dryer used in tea drying processes in presence of induced magnetic field. A mathematical model describing the fluid flow in a Fluidized bed dryer was developed using the nonlinear partial differential equations. Due to their non-linearity, the equations were solved numerically by use of the finite difference method. The effects of physical flow parameters on velocity, temperature, concentration and magnetic induction profiles were studied and results were presented graphically. From the mathematical analysis, it was deduced that addition of silver nanoparticles into the fluid flow enhanced velocity and temperature profiles. This led to improved heat transfer in the fluidized bed dryer, hence amplifying the tea drying process. Furthermore, it was noted that induced magnetic field tends to decrease the fluid velocity, which results in uniform distribution of heat leading to efficient heat transfer between the tea particles and the fluid, thus improving the drying process. The research findings provide information to industries on ways to optimize thermal performance of fluidized bed dryers.

Keywords

Heat Transfer, Induced Magnetic Field, Nanofluid, Fluidized Bed Dryer

1. Introduction

Tea is one of the major agricultural activities practiced in most parts of the world such as China, India, Sri Lanka and Japan [1]. Drying is one of the steps in tea processing, which uses thermal and electric energies for heat and mass transfer resulting in temperature gain or mass loss. Drying of tea particles is a complex

problem encountered in the field of engineering. Fluid bed dryers are used in drying processes. It works under the principle of fluidization where hot air is passed at higher pressure through a perforated stainless steel chamber with tea leaves to be dried. Tea drying process is an energy-intensive operation that represents significant amount of production costs. To reduce the energy expenses associated with drying processes in tea processing industries, it is important to consider research on heat and mass transfer within the fluidized bed dryer. The study of heat and mass transfer processes aids in designing energy-efficient dryers. The objective of modeling heat and mass transfer processes during tea drying is to provide more insights into the transport phenomena within the dryer during fluidization and optimize the drying process. Studies done in the past on heat and mass transfer in fluidized bed dryers have aimed to enhance their thermodynamic processes. There are various ways of modeling heat and mass transfer processes in fluidized bed dryer.

[2] in their research introduced a technique for determining the heat transfer coefficient during the constant drying rate stage using drying data. They assumed that the degree of fluidization guarantees ideal mixing for both the solid and the drying medium phases. They observed that the heat transfer coefficient measured during drying experiments was significantly lower than the coefficient computed from empirical relationships in existing literature based on experiments. This discrepancy could have significant implications for equipment design and operational decision-making. The study by [3] investigated the modeling and control of moisture content in particles during batch-fluidized bed drying. Initially, a lumped mechanistic model was created to describe heat and mass transfer between the solid, gas, and bubble phases. The model was validated experimentally and found to accurately predict particle moisture content and temperature profiles during the drying process. The impact of wall temperature on the drying process was also investigated by validating the model with and without an insulator on the dryer wall. Feedback control of material moisture content was then explored using tomographic sensors in the control loop, and a controller was designed to achieve a desired drying rate. Simulations demonstrated successful control of the drying rate. The lumped dynamic model was shown to improve bed dryer efficiency, with experimental validation supporting its accuracy. The inclusion of moisture content measurement in the control loop simplified the design process, and a simple PI controller was found to be effective for controlling a batch-fluidized bed dryer. [4] developed a mathematical model for batch-fluidized bed drying by considering the temperature, moisture saturation and pressure distributions in the particle. They derived and analysed a new variable called bed area factor from the differential equations. The study showed that the bed area factor was important in determining the drying efficiency and operation of fluidized bed dryers. An increase in bed area factor had significant effect on gas efficiency however, when bed factor was small, load of materials needed to be increased to raise the drying efficiency.

The study conducted by [5] employed CFD-DEM to investigate multiple aspects of a 2D fluidized bed dryer, such as aerodynamics, temperature distribution, and heat transfer. They utilized Navier Stokes equations and energy equations to analyze the minimum fluidization velocity, temperature, and heat transfer coefficient. The outcomes were then compared to experimental data, which revealed slight variations in temperature profiles and a slightly elevated predicted heat transfer coefficient. Nevertheless, the authors determined that the CFD-DEM model was successful in forecasting the minimum fluidization velocity, and the data obtained from the investigation was advantageous in designing and improving fluidized bed dryers. A study by [6] focused on a 2D mathematical model to simulate simultaneous heat and mass transfer during porous media drying, using Whitaker's theory. The model was based on cylindrical coordinates, which were deemed more practical than spherical coordinates. Fluidized-bed drying conditions were simulated numerically using the fully implicit control-volume method to discretize governing equations. The study analyzed heat and mass transfer mechanisms by examining temperature and saturation profiles within the particles. Simulation results revealed that coupled heat and mass transfer between the gas and solid phases significantly affected the drying process. The drying time increased with temperature and velocity of the inlet gas, while it decreased with humidity and bed area factor.

[7] proposed mathematical model to explore the impact of operational parameters on simultaneous heat and mass transfer in a fluidized bed dryer. The aim was to enhance the accuracy of fluidized bed drying modeling through volumetric transfer coefficients. The model required volumetric heat transfer coefficients and was able to calculate the temperature and absolute humidity of the drying gas, as well as the temperature and moisture content of the material over time. [8] proposed and investigated a FBD that drys tea in three stages by use of energy and exergy analysis. They were able to determine various properties that affect thermal efficiency of FBD. They noted that an increase in the amount of dried tea increased the drier's efficiency. However, an increase in temperature and the flow rate of drying air lead to an increase in exergy destruction hence decreasing the dryer's efficiency. Furthermore, the the efficiency of FBD in terms of exergy and energy was found to be 7.2% and 42% respectively.

[9] used FVM to study the effect of external magnetic field on the nanofluid flow inside a heat exchanger. The influence of the variation of different parameters such as geometric shape, intensity of magnetic field and Reynolds number on heat transfer was considered. The results showed that the presence of magnetic field increased the heat transfer significantly, which in turn increased the performance of the heat exchanger. [10] introduced nanoparticles and constant magnetic in porous medium to investigate heat and mass transfer of natural convection MHD flow. By use of similarity solution, the study determined fluid flow profiles and examined the effect of parameters on flow field. The study noted that an increase in magnetic field caused a decrease in velocity but and an increase in concentration and temperature profiles. Furthermore, high mass transfer rate was

strongly influenced by the concentration and temperature boundary layer thickness. [11] numerically investigated effects of magnetic field on forced convection by considering a partitioned cylinder in a porous medium. The walls of the cylindrical geometry were assumed to have constant and uniform heat flux. The study found that addition of nanoparticles increased the mass transfer rate while increase in magnetic field improved the performance evaluation criteria inside a cylinder containing a porous medium.

Tea processing industries majorly use fluidized bed dryers which is an energy-intensive drying process. Heat and mass transfer processes in fluidized bed dryer is a complex process due to the interaction of tea particles and hot air during fluidization. Previous studies analysed heat and mass transfer in fluidized bed dryer by considering parameters that led to energy loss or increase. Others have designed and developed fluidized bed dryers with the aim of saving energy costs while others have investigated the effects of air velocity, particle size and bed height on the drying process in fluidized bed dryers. Drying process consumes a lot of energy compared to other processes during tea production hence the need to come up with sustainable and energy-efficient methods that utilize energy optimally. Therefore, there is a need for research on the combined effects of magnetic fields and nanoparticles on the drying process. This research thus explores the impact of magnetic field and addition of nanoparticles on heat distribution and the fluidization process in fluidized bed dryers by developing a mathematical model that can describe heat and mass transfer process during fluidization, taking into account magnetic field and nanoparticles with the aim of improving the efficiency of tea drying processes, reduce energy consumption and produce high-quality dried tea products. In line with the existing literature, this study focused on first developing a hydromagnetic mathematical model in presence of nanoparticles in a fluidized bed dryer. The model involves non-linear partial differential equations which are solved using the Finite Difference Method. Lastly, the effects of fluid flow parameters on various flow profiles are presented in a graphical form.

2. Mathematical Model

The study examines the dynamics of a hydromagnetic nanofluid flow in a fluidized bed dryer. It considers the following assumptions: the flow is two-dimensional, unsteady, laminar, axisymmetric and incompressible in nature. The flow is characterized by velocities in z and r directions where $\boldsymbol{V}=\left(v_r,0,v_z\right)$ is the velocity vector of the fluid flow and $\boldsymbol{B}=\left(B_r,0,B_z\right)$ is the magnetic field vector in $\left(r,\theta,z\right)$ directions. A constant magnetic field B_0 is applied perpendicular to the flow as shown in **Figure 1**. The fluid concentration and temperature at the bed is denoted by C_b and T_b respectively such that $C_b<C_\infty$ and $T_b>T_\infty$.

The flow within the fluidized bed dryer is governed by the nonlinear partial differential equations. Boussinesq approximation is applied as a simplifying

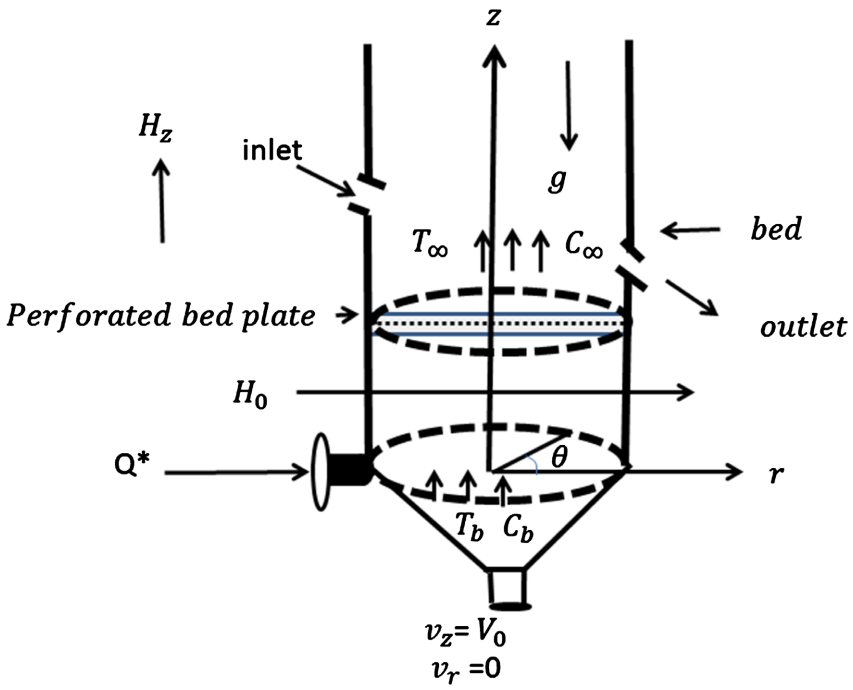

Figure 1. Physical model of FBD and coordinate system.

assumption to neglect small variations in fluid density, except in instances where there is a significant impact as a buoyancy term represented by $\rho_{nf} g$. The pressure gradient is evaluated at the boundary layer where the fluid velocity is at its minimum and the density approaches a constant value, $\rho_{\infty nf}$, as the velocity approaches zero. The pressure term in the axial direction is then expressed as:

$$-\frac{\partial P}{\partial z} = -g\rho_{\infty nf} \tag{1}$$

By combining this pressure gradient result with gravitational body force term in axial direction, it gives:

$$F_b = -g\rho_{\infty nf} + \rho_{nf} g = g\left(\rho_{nf} - \rho_{\infty nf}\right) \tag{2}$$

Mathematically, the density variations are assumed to be given by:

$$\rho_{nf} \approx \rho_{\infty_{nf}} + \frac{\partial \rho}{\partial T}\left(T_b - T_\infty\right) + \frac{\partial \rho}{\partial C}\left(C_\infty - C_b\right) \tag{3}$$

Substituting the Boussinesq approximation given by Equation (3) into Equation (2) yields:

$$F_b = g\left(\frac{\partial \rho}{\partial T}\left(T_b - T_\infty\right) + \frac{\partial \rho}{\partial C}\left(C_\infty - C_b\right)\right) \tag{4}$$

Thermal expansion coefficient due to temperature difference is given by:

$$\beta_{Tnf} = -\frac{1}{\rho_{nf}}\frac{\partial \rho_{nf}}{\partial T} \tag{5}$$

while the thermal expansion coefficient resulting from concentration difference is expressed as:

$$\beta_{Cnf} = -\frac{1}{\rho_{nf}}\frac{\partial \rho_{nf}}{\partial C} \tag{6}$$

Rewriting the buoyancy force Equation (4) using the thermal and concentration coefficients above results in buoyancy force per unit volume expressed as:

$$F_b = -\boldsymbol{g}\rho_{nf}\left(\beta_{Tnf}\left(T_b - T_\infty\right) + \beta_{Cnf}\left(C_b - C_\infty\right)\right) \tag{7}$$

The gravitational force in the radial direction has no significant impact on the nanofluid flow, hence $\rho_{nf} g_r = 0$. Thus in the radial direction, the only body force that is considered is the Lorentz force $\boldsymbol{F}_{EM}$, which arises from the interaction between the magnetic field and the electrically charged particles in the fluid. Since the gravitational force acts in the direction opposite to the flow and is parallel to the z axis, it is taken into account along with the Lorentz force in the axial direction of fluid flow. The Mathematical form of Lorentz force is given as (see [12]):

$$\boldsymbol{F}_{EM} = \boldsymbol{J} \times \boldsymbol{B} \tag{8}$$

From Ohm's law,

$$\boldsymbol{J} = \sigma_{nf}\left(\boldsymbol{E} + \boldsymbol{V} \times \boldsymbol{B}\right) \tag{9}$$

and assuming applied electric field $\boldsymbol{E}$ is negligible then,

$$\begin{aligned} \boldsymbol{J} = \sigma_{nf}\left(\boldsymbol{V} \times \boldsymbol{B}\right) &= \begin{vmatrix} \boldsymbol{e}_r & \boldsymbol{e}_\theta & \boldsymbol{e}_z \\ v_r & 0 & v_z \\ B_0 + B_r & 0 & B_z \end{vmatrix} \\ &= \sigma_{nf}\left[vz\left(B_0 + B_r\right) - v_r B_z\right]\boldsymbol{e}_\theta \end{aligned} \tag{10}$$

Hence,

$$F_{EM} = \boldsymbol{J} \times \boldsymbol{B} = \sigma_{nf}\begin{vmatrix} \boldsymbol{e}_r & \boldsymbol{e}_\theta & \boldsymbol{e}_z \\ 0 & v_z\left(B_0 + B_r\right) - v_r B_z & 0 \\ B_0 + B_r & 0 & B_z \end{vmatrix} \tag{11}$$

Since

$$B = \mu_e H,\ \boldsymbol{B} = \left(B_r, 0, B_z\right) \text{ and } \boldsymbol{H} = \left(H_0, 0, H_z\right) \tag{12}$$

Using the above relation, we obtain:

$$\begin{aligned} \boldsymbol{F}_{EM} = \boldsymbol{J} \times \boldsymbol{B} = \sigma_{nf}\mu_e^2\left[v_z\left(H_r H_z + H_0 H_z\right) - v_r H_z^2\right]\boldsymbol{e}_r \\ + \sigma_{nf}\mu_e^2\left[v_r\left(H_0 H_z + H_z H_r\right) - v_z\left(H_r^2 + 2H_0 H_r + H_0^2\right)\right]\boldsymbol{e}_z \end{aligned} \tag{13}$$

The mathematical model thus considers additional body forces (magnetic and buoyancy) in momentum equations. Additionally, the model also considers introduction of radiative heat flux in equation of energy. The radiative heat flux is obtained from Rosseland's approximation, which is a simplified model used to estimate the radiative heat transfer in a medium. [13] expressed it as follows:

$$q_r = -\frac{4\sigma^*}{3k^*}\frac{\partial T^4}{\partial r} \tag{14}$$

In Equation (14), σ^* is Stefan-Boltzmann constant and k^* the mean absorp-

tion coefficient. Temperature T^4 is approximated as a linear function of T, which is obtained by use of Taylor series expansion around T_∞ given by:

$$T^4 = T_\infty^4 + 4T_\infty^3\left(T - T_\infty\right) + \mathcal{O}\left(T - T_\infty\right)^2 \tag{15}$$

Substituting (15) in Equation (14) reduces to:

$$q_r \approx -\frac{16\sigma^*}{3k^*}T_\infty^3\frac{\partial T}{\partial r} \tag{16}$$

The specific nonlinear partial differential equations governing the flow in cylindrical coordinates are given as follows:

Equation of Continuity:

$$\frac{1}{r}\frac{\partial\left(rv_r\right)}{\partial r} + \frac{\partial v_z}{\partial z} = 0 \tag{17}$$

Momentum equation in r direction:

$$\begin{aligned}\rho_{nf}\left(\frac{\partial v_r}{\partial t} + v_r\frac{\partial v_r}{\partial r} + v_z\frac{\partial v_r}{\partial z}\right) = -\frac{\partial P}{\partial r} + \mu_{nf}\left(\frac{\partial^2 v_r}{\partial r^2} + \frac{1}{r}\frac{\partial v_r}{\partial r} + \frac{\partial^2 v_r}{\partial z^2} - \frac{v_r}{r^2}\right)\\ + \sigma_{nf}\mu_e^2\left(v_z\left(H_r H_z + H_0 H_z\right) - v_r H_z^2\right)\end{aligned} \tag{18}$$

Momentum equation in z direction:

$$\begin{aligned}&\rho_{nf}\left(\frac{\partial v_z}{\partial t} + v_r\frac{\partial v_z}{\partial r} + v_z\frac{\partial v_z}{\partial z}\right)\\ &= \mu_{nf}\left(\frac{\partial^2 v_z}{\partial r^2} + \frac{1}{r}\frac{\partial v_z}{\partial r} + \frac{\partial^2 v_z}{\partial z^2}\right) - g\rho_{nf}\left(\beta_{Tnf}\left(T_b - T_\infty\right) + \beta_{Cnf}\left(C_b - C_\infty\right)\right)\\ &\quad + \sigma_{nf}\mu_e^2\left(v_r\left(H_0 H_z + H_z H_r\right) - v_z\left(H_r^2 + 2H_0 H_r + H_0^2\right)\right)\end{aligned} \tag{19}$$

Energy equation:

$$\begin{aligned}&\left(\rho C_p\right)_{nf}\left(\frac{\partial T}{\partial t} + v_r\frac{\partial T}{\partial r} + v_z\frac{\partial T}{\partial z}\right)\\ &= k_{nf}\left[\frac{1}{r}\frac{\partial}{\partial r}\left(r\frac{\partial T}{\partial r}\right) + \frac{\partial^2 T}{\partial z^2}\right] + \mu_{nf}\left(2\left[\left(\frac{\partial v_r}{\partial r}\right)^2 + \left(\frac{\partial v_z}{\partial z}\right)^2\right] + \left(\frac{\partial v_r}{\partial z} + \frac{\partial v_z}{\partial r}\right)^2\right)\\ &\quad - \frac{16\sigma^*}{3k^*}T_\infty^3\frac{\partial T}{\partial r} + Q^*\left(T_b - T_\infty\right)\end{aligned} \tag{20}$$

Concentration equation:

$$\frac{\partial C}{\partial t} + v_r\frac{\partial C}{\partial r} + v_z\frac{\partial C}{\partial z} = D_{nf}\left(\frac{\partial^2 C}{\partial r^2} + \frac{\partial^2 C}{\partial z^2}\right) - k_r\left(C_\infty - C_b\right) \tag{21}$$

Magnetic induction equation in r direction

$$\frac{\partial H_r}{\partial t} = v_r\frac{\partial H_z}{\partial z} + H_z\frac{\partial v_r}{\partial z} - H_0\frac{\partial v_z}{\partial z} - v_z\frac{\partial H_r}{\partial z} - H_r\frac{\partial v_z}{\partial z} + \eta\frac{1}{r}\frac{\partial}{\partial r}\left(r\frac{\partial H_r}{\partial r}\right) \tag{22}$$

Magnetic induction equation in z direction:

$$\frac{\partial H_z}{\partial t} = H_0\frac{\partial v_z}{\partial r} + H_r\frac{\partial v_z}{\partial r} + v_z\frac{\partial H_r}{\partial r} - H_z\frac{\partial v_r}{\partial r} - v_r\frac{\partial H_z}{\partial r} + \eta\frac{\partial^2 H_z}{\partial z^2} \tag{23}$$

The thermophysical properties of nanofluid as defined by [14] are as follows:
Dynamic viscosity of nanofluid:

$$\mu_{nf} = \frac{\mu_f}{(1-\phi)^{2.5}} \tag{24}$$

Nanofluid density:

$$\rho_{nf} = (1-\phi)\rho_f + \phi\rho_s \tag{25}$$

Nanofluid thermal expansion coefficient:

$$\beta_{nf} = (1-\phi)\beta_f + \phi\beta_s \tag{26}$$

Heat capacitance of nanofluid:

$$(\rho C_p)_{nf} = (1-\phi)(\rho C_p)_f + \phi(\rho C_p)_s \tag{27}$$

Nanofluid effective thermal conductivity:

$$\frac{k_{nf}}{k_f} = \frac{(k_s + 2k_f) - 2\phi(k_f - k_s)}{(k_s + 2k_f) + \phi(k_f - k_s)} \tag{28}$$

Electrical conductivity:

$$\sigma_{nf} = (1-\phi)\sigma_f + \phi\sigma_s \tag{29}$$

The governing equations are solved simultaneously subject to the following initial and boundary conditions:

$$\begin{aligned}
&t \geq 0 : r = 0 :\ v_r = 0,\ \frac{\partial v_z}{\partial z} = 0,\ H_r = 0,\ H_z = H_0 \\
&r_{\text{wall}} = R :\ v_r = 0,\ v_z = 0,\ T = T_b,\ C = C_b,\ T_\infty > T_b,\ C_\infty < C_b,\ H_r = 0,\ H_z = 0 \\
&z = 0 :\ T = T_b,\ C = C_b,\ v_z = 0,\ H_r = 0,\ H_z = 0 \\
&z = z_{\max} :\ T = T_\infty,\ C = C_\infty,\ v_z \to v_\infty = 0,\ H_r = 0,\ H_z = 0
\end{aligned} \tag{30}$$

The equations that govern the flow are non-dimensionalized using the following transformations:

$$\begin{aligned}
&v_r^* = \frac{v_r}{U},\ v_z^* = \frac{v_z}{U},\ r^* = \frac{r}{R},\ P^* = \frac{P}{\rho U^2},\ t^* = \frac{Ut}{R},\ z^* = \frac{z}{R},\ T^* = \frac{T - T_\infty}{T_b - T_\infty} \\
&C^* = \frac{C - C_\infty}{C_b - C_\infty},\ H_z^* = \frac{H_z}{H_0},\ H_r^* = \frac{H_r}{H_0}
\end{aligned} \tag{31}$$

and the expressions below represent the non-dimensional parameters:

$$\begin{aligned}
&Re = UR\frac{\rho_f}{\mu_f},\ M = \frac{H_0^2 \mu_e^2 \sigma R^2}{\nu\rho},\ Gr_T = \frac{R\boldsymbol{g}\beta_{Tf}(T_b - T_\infty)}{U^2},\ \Omega = \frac{Q^*}{U(\rho C_p)_f}, \\
&K_1 = k_r\frac{R}{U},\ Gr_C = \frac{R\boldsymbol{g}\beta_{Cf}(C_b - C_\infty)}{U^2},\ Pr = \frac{\nu(\rho C_p)_f}{k_f},\ Ec = \frac{U^2}{C_{pf}(T_b - T_\infty)}, \\
&Sc = \frac{\nu}{D_{nf}},\ Pr_M = \mu_f\sigma_f\nu
\end{aligned} \tag{32}$$

Thus, Equations (18)-(23) in dimensionless form are given as follows:

$$\frac{\partial v_r^*}{\partial t^*}+v_r^*\frac{\partial v_r^*}{\partial r^*}+v_z^*\frac{\partial v_r^*}{\partial z^*}=-\frac{\partial P^*}{\partial r^*}+\frac{\phi_1}{Re}\left(\frac{\partial^2 v_r^*}{\partial r^{*2}}+\frac{1}{r^*}\frac{\partial v_r^*}{\partial r^*}-\frac{v_r^*}{r^{*2}}+\frac{\partial^2 v_r^*}{\partial z^{*2}}\right)+\phi_2\frac{M}{Re}\left(v_z^*\left(H_z^*\left(H_r^*+1\right)\right)-v_r^* H_z^{*2}\right) \tag{33}$$

$$\frac{\partial v_z^*}{\partial t^*}+v_r^*\frac{\partial v_z^*}{\partial r^*}+v_z^*\frac{\partial v_z^*}{\partial z^*}=\frac{\phi_1}{Re}\left(\frac{\partial^2 v_z^*}{\partial r^{*2}}+\frac{1}{r^*}\frac{\partial v_z^*}{\partial r^*}+\frac{\partial^2 v_z^*}{\partial z^{*2}}\right)-\phi_3 G_{rT}-\phi_3 G_{rC}+\phi_2\frac{M}{Re}\left(v_r^*\left(H_z^*\left(1+H_r^*\right)\right)-v_z^*\left(H_r^{*2}+2H_r^*+1\right)\right) \tag{34}$$

$$\frac{\partial T^*}{\partial t^*}+v_r^*\frac{\partial T^*}{\partial r^*}+v_z^*\frac{\partial T^*}{\partial z^*}=\phi_4\frac{1}{Pr}\frac{1}{Re}\left[\frac{1}{r^*}\frac{\partial}{\partial r^*}\left(r^*\frac{\partial T^*}{\partial r^*}\right)+\frac{\partial^2 T^*}{\partial z^{*2}}\right]+\phi_5\frac{Ec}{Re}\left(2\left[\left(\frac{\partial v_r^*}{\partial r^*}\right)^2+\left(\frac{\partial v_z^*}{\partial z^*}\right)^2\right]+\left(\frac{\partial v_r^*}{\partial z^*}+\frac{\partial v_z^*}{\partial r^*}\right)^2\right)-\phi_6\frac{q_r}{PrRe}+\phi_6\Omega \tag{35}$$

$$\frac{\partial C^*}{\partial t^*}+v_r^*\frac{\partial C^*}{\partial r^*}+v_z^*\frac{\partial C^*}{\partial z^*}=\frac{1}{Sc}\frac{1}{Re}\left(\frac{\partial^2 C^*}{\partial r^{*2}}+\frac{\partial^2 C^*}{\partial z^{*2}}\right)-K_1 \tag{36}$$

$$\frac{\partial H_r^*}{\partial t^*}=v_r^*\frac{\partial H_z^*}{\partial z^*}+H_z^*\frac{\partial v_r^*}{\partial z^*}-\left(1+H_r^*\right)\frac{\partial v_z^*}{\partial z^*}-v_z^*\frac{\partial H_r^*}{\partial z^*}+\frac{1}{\phi_7}\frac{1}{Pr_M}\frac{1}{Re}\frac{1}{r^*}\frac{\partial}{\partial r^*}\left(r^*\frac{\partial H_r^*}{\partial r^*}\right) \tag{37}$$

$$\frac{\partial H_z^*}{\partial t^*}=\left(1+H_r^*\right)\frac{\partial v_z^*}{\partial r^*}+v_z^*\frac{\partial H_r^*}{\partial r^*}-H_z^*\frac{\partial v_r^*}{\partial r^*}-v_r^*\frac{\partial H_z^*}{\partial r^*}+\frac{1}{\phi_7}\frac{1}{Pr_M}\frac{1}{Re}\frac{\partial^2 H_z^*}{\partial z^{*2}} \tag{38}$$

ϕ_1 to ϕ_7 are obtained from the thermophysical properties of nanofluid where $\phi=0$ refers to regular fluid. The dimensionless intial and boundary conditions are given as:

$$\begin{aligned}
&t\geq 0: r^*=0: \ v_r^*=0,\ \frac{\partial v_z^*}{\partial z^*}=f\left(z^*\right),\ \frac{\partial T^*}{\partial z^*}=g\left(z^*\right),\ \frac{\partial C^*}{\partial z^*}=h\left(z^*\right),\ H_r^*=0,\ H_z^*=1\\
&r_{\text{wall}}^*=1: \ v_r^*=0,\ v_z^*=0,\ T^*=1,\ C^*=1,\ H_r^*=0,\ H_z^*=0\\
&z=0: \ T^*=1,\ C^*=1\ v_z^*=0,\ H_r^*=0,\ H_z^*=0\\
&z=z_{\max}: \ T^*=0,\ C^*=0,\ v_z^*=0,\ H_r^*=0,\ H_z^*=0
\end{aligned} \tag{39}$$

3. Methodology

The finite difference method is a numerical technique used to solve differential equations by approximating derivatives using finite differences. The continuous domain is divided into a uniform grid, which is a finite number of discrete points. The physical domain is divided by use of finite difference mesh to obtain finite discrete approximations in relation to time and space domains. A mesh of uniform rectangles with sides Δr and Δz representing changes in the radial (r) and axial (z) directions respectively is used. This discretization allows the problem to be implemented on a computer by use of MATLAB subject to the initial and

boundary conditions. For our governing equations given in (33)-(36) and (38), a finite difference scheme (forward time, central space) is used to obtain the set of finite difference equations.

Momentum equation in r direction:

$$\begin{aligned} U_{j,k}^{i+1} = \Delta t\Bigg\{ & -U_{j,k}^{i}\left(\frac{U_{j+1,k}^{i}-U_{j-1,k}^{i}}{2\Delta r}\right)-V_{j,k}^{i}\left(\frac{U_{j,k+1}^{i}-U_{j,k-1}^{i}}{2\Delta z}\right)-\varphi \\ & +\frac{\phi_1}{Re}\Bigg(\frac{U_{j+1,k}^{i}-2U_{j,k}^{i}+U_{j-1,k}^{i}}{(\Delta r)^2}+\frac{U_{j+1,k}^{i}-U_{j-1,k}^{i}}{2r\Delta r} \\ & -\frac{U_{j,k}^{i}}{r^2}+\frac{U_{j,k+1}^{i}-2U_{j,k}^{i}+U_{j,k-1}^{i}}{(\Delta z)^2}\Bigg) \\ & +\phi_2\frac{M}{Re}\Big(V_{j,k}^{i}\left(H_{z\,j,k}^{\ i}\left(H_{r\,j,k}^{\ i}+1\right)\right)-U_{j,k}^{i}H_{z\,j,k}^{2i}\Big)\Bigg\}+U_{j,k}^{i} \end{aligned} \tag{40}$$

Momentum equation in z direction:

$$\begin{aligned} V_{j,k}^{i+1} = \Delta t\Bigg\{ & -U_{j,k}^{i}\left(\frac{V_{j+1,k}^{i}-V_{j-1,k}^{i}}{2\Delta r}\right)-V_{j,k}^{i}\left(\frac{V_{j,k+1}^{i}-V_{j,k-1}^{i}}{2\Delta z}\right) \\ & +\frac{\phi_1}{Re}\Bigg(\frac{V_{j+1,k}^{i}-2V_{j,k}^{i}+V_{j-1,k}^{i}}{(\Delta r)^2}+\frac{1}{r}\frac{V_{j+1,k}^{i}-V_{j-1,k}^{i}}{2\Delta r}+\frac{V_{j,k+1}^{i}-2V_{j,k}^{i}+V_{j,k-1}^{i}}{(\Delta z)^2}\Bigg) \\ & -\phi_3 Gr_T-\phi_3 Gr_C+\phi_2\frac{M}{Re}\Big(U_{j,k}^{i}\left(H_{z\,j,k}^{\ i}\left(1+H_{r\,j,k}^{\ i}\right)\right) \\ & -V_{j,k}^{i}\left(H_{r\,j,k}^{2i}+2H_{r\,j,k}^{\ i}+1\right)\Big)\Bigg\}+V_{j,k}^{i} \end{aligned} \tag{41}$$

Energy equation:

$$\begin{aligned} T_{j,k}^{i+1} = \Delta t\Bigg\{ & -U_{j,k}^{i}\left(\frac{T_{j+1,k}^{i}-T_{j-1,k}^{i}}{2\Delta r}\right)-V_{j,k}^{i}\left(\frac{T_{j,k+1}^{i}-T_{j,k-1}^{i}}{2\Delta z}\right) \\ & +\frac{\phi_4}{PrRe}\Bigg(\frac{1}{r}\frac{T_{j+1,k}^{i}-T_{j-1,k}^{i}}{2\Delta r}+\frac{T_{j+1,k}^{i}-2T_{j,k}^{i}+T_{j-1,k}^{i}}{(\Delta r)^2}+\frac{T_{j,k+1}^{i}-2T_{j,k}^{i}+T_{j,k-1}^{i}}{(\Delta z)^2}\Bigg) \\ & +\phi_5\frac{Ec}{Re}\Bigg(2\left[\left(\frac{U_{j+1,k}^{i}-U_{j-1,k}^{i}}{2\Delta r}\right)^2+\left(\frac{V_{j,k+1}^{i}-V_{j,k-1}^{i}}{2\Delta z}\right)^2\right] \\ & +\left(\frac{U_{j,k+1}^{i}-U_{j,k-1}^{i}}{2\Delta z}+\frac{V_{j+1,k}^{i}-V_{j-1,k}^{i}}{2\Delta r}\right)^2\Bigg)+\phi_6\left(\Omega-\frac{q_r}{PrRe}\right)\Bigg\}+T_{j,k}^{i} \end{aligned} \tag{42}$$

Equation of concentration:

$$\begin{aligned} C_{j,k}^{i+1} = \Delta t\Bigg\{ & -U_{j,k}^{i}\left(\frac{C_{j+1,k}^{i}-C_{j-1,k}^{i}}{2\Delta r}\right)-V_{j,k}^{i}\left(\frac{C_{j,k+1}^{i}-C_{j,k-1}^{i}}{2\Delta z}\right) \\ & +\frac{1}{ScRe}\Bigg(\frac{C_{j+1,k}^{i}-2C_{j,k}^{i}+C_{j-1,k}^{i}}{(\Delta r)^2}+\frac{C_{j,k+1}^{i}-2C_{j,k}^{i}+C_{j,k+1}^{i}}{(\Delta z)^2}\Bigg)-K_1\Bigg\}+C_{j,k}^{i} \end{aligned} \tag{43}$$

Magnetic Induction Equation in r direction:

$$H_{j,k}^{i+1}=\Delta t\left\{V_{j,k}^{i}\left(\frac{H_{j,k+1}^{i}-H_{j,k}^{i}}{2\Delta z}\right)+H_{j,k}^{i}\left(\frac{U_{j,k+1}^{i}-U_{j,k}^{i}}{2\Delta z}\right)\right.$$
$$\left.-\left(1+H_{j,k}^{i}\right)\left(\frac{V_{j,k+1}^{i}-V_{j,k}^{i}}{2\Delta z}\right)-V_{j,k}^{i}\left(\frac{H_{j,k+1}^{i}-H_{j,k}^{i}}{2\Delta z}\right)\right\} \tag{44}$$
$$+\frac{\Delta t}{\phi_7}\frac{1}{P_{rm}Re}\left(\frac{H_{j+1,k}^{i}-H_{j-1,k}^{i}}{2r\Delta r}+\frac{H_{j+1,k}^{i}-2H_{j,k}^{i}+H_{j-1,k}^{i}}{\left(\Delta r\right)^2}\right)+H_{j,k}^{i}$$

Magnetic induction equation in z direction:

$$H_{j,k}^{i+1}=\Delta t\left\{\left(1+H_{j,k}^{i}\right)\frac{V_{j+1,k}^{i}-V_{j-1,k}^{i}}{2\Delta r}+V_{j,k}^{i}\frac{H_{j+1,k}^{i}-H_{j-1,k}^{i}}{2\Delta r}-H_{j,k}^{i}\frac{U_{j+1,k}^{i}-U_{j-1,k}^{i}}{2\Delta r}\right.$$
$$\left.-V_{j,k}^{i}\frac{H_{j+1,k}^{i}-H_{j-1,k}^{i}}{2\Delta r}\right\}+\frac{\Delta t}{\phi_7}\frac{1}{P_{rm}Re}\left(\frac{H_{j,k+1}^{i}-2H_{j,k}^{i}+H_{j,k-1}^{i}}{\left(\Delta z\right)^2}\right)+H_{j,k}^{i} \tag{45}$$

The corresponding initial and boundary conditions are:

$$t\geq 0:\ \text{At}\ \ r^{*}=0: U_{j,k}^{i+1}=0,\ \frac{V_{j,k+1}^{i}-V_{j,k}^{i}}{\Delta z}=f\left(z\right),\ \frac{T_{j,k+1}^{i}-T_{j,k}^{i}}{\Delta z}=g\left(z\right),$$
$$\frac{C_{j,k+1}^{i}}{\Delta z}=h\left(z\right),\ H_{r0,k}^{i+1}=0,\ H_{z0,k}^{i+1}=1$$
$$r_{\text{wall}}^{*}=1:\ U_{j,k}^{i+1}=0,\ V_{j,k}^{i+1}=0,\ T_{j,k}^{i+1}=1\ C_{j,k}^{i+1}=1\ H_{r\,j,k}^{i+1}=0,\ H_{z\,j,k}^{i+1}=0 \tag{46}$$
$$z=0:\ T_{j,k}^{i+1}=1,\ C_{j,k}^{i+1}=1,\ V_{j,k}^{i+1}=0,\ H_{r\,j,0}^{i+1}=0,\ H_{z\,j,0}^{i+1}=0$$
$$z=z_{\max}:\ T_{j,k}^{i+1}=0,\ C_{j,k}^{i+1}=0,\ V_{j,k}^{i+1}=0,\ B_{r\,j,k}^{i+1}=0,\ H_{z\,j,k}^{i+1}=0$$

In this study, we adopt the von Neumann method to analyse the stability of the finite difference equations. To perform the the stability analysis, we assume a numerical solution which takes the following form:

$$C_{j,k}^{i}=G^{i}\mathrm{e}^{i\left(j\Delta r+k\Delta z\right)} \tag{47}$$

where G is the amplification factor which helps one to determine the growth or decay of errors in the finite difference method. It represents how errors are amplified at each time step of the computation. If $\left|G\right|>1$ it means that errors grow at each time step of the computation and the finite difference scheme is unstable. If $\left|G\right|\leq 1$ it implies that errors do not grow and the numerical solution remains bounded and convergent over time, thus stable numerical scheme. Therefore, to achieve stability of the finite difference scheme $\left|G\right|\leq 1$. From the simulation, the amplification factor G was found to have the values less than 1 as follows 0.034, −6.6841, −9.815, −9.6094, −4.1113, −8.6796, −4.0301, −2.3652 and then it tends to 0. This indicates that the numerical method used does not amplify the errors uncontrollably and the results obtained are reliable. The relationship between stability and convergence of finite difference method can be asserted by Lax Equivalence theorem which states that under appropriate boundary conditions a numerical scheme is convergent if and only if it is stable [15].

4. Results and Discussion

The effect of various flow parameters on velocity, temperature, concentration and induced magnetic field profiles are presented in graphical form. This was done by varying various parameters to investigate how they affect the flow profiles. Prandtl number ($Pr = 0.71$-air gas) was kept constant for all computations.

4.1. Velocity Profiles

In **Figure 2(a)**, the primary velocity profiles increases as the Reynolds number increases. Reynold number describes the ratio of inertial forces to viscous forces. As the Reynolds number increases, the inertial forces become dominant and viscous forces are weakened. The role of viscous forces becomes less significant in the fluid flow which leads to reduction of boundary layer thickness. Thinner boundary layers have less resistance to flow leading to lower drag force. Moreover, when inertial forces become more dominant it promotes better fluidization and increased velocities. The negative values of the secondary velocity profiles in the radial direction show that the fluid is moving in the opposite direction of the primary flow as a result of centrifugal forces that push the fluid towards the walls of the dryer. At the walls of the dryer, the velocity is zero as a result of the no slip condition.

As the Hartmann number increases, there is a decrease in the primary flow velocity profiles as seen in **Figure 3**. Hartmann number represents the ratio of magnetic to viscous forces. Increase in Hartmann number indicates stronger magnetic field and decrease in the influence of viscous forces. Increase in Hartmann number implies stronger magnetic field leading to an increase in resistive force caused by Lorentz force opposing the fluid flow. This leads to reduction of the boundary layer thickness which corresponds to decrease of the influence of the viscous forces on the fluid flow. The general effect of this resistive force is that it slows down the velocity of the fluid leading to overall decrease in velocity distribution of the fluid flow in the dryer. The modification of fluid flow due to the presence of induced magnetic field has an effect on the transport of the tea particles within the dryer. As magnetic field increases, tea particles experience Lorentz force which may alter the residence time in the drying zone. Reduced velocities help to optimize the drying process and ensure that the tea particles are exposed to appropriate drying conditions within the dryer so as to achieve the desired improved yields.

Figure 4(a) depicts that increase in local temperature Grashof number leads to a rise in primary velocity profiles. Local temperature Grashof number quantifies the ratio of thermal buoyancy force to viscous forces in a flow. This is because increase in Grashof number leads to stronger thermal buoyant force which drives the fluid. Local temperature Grashof number is related to heating of the fluid or cooling of the dryer's walls which results in temperature gradient within the fluid. When thermal Grashof number is high, temperature difference in the fluid is significant leading to free convection currents. Thus, velocity of the fluid increases

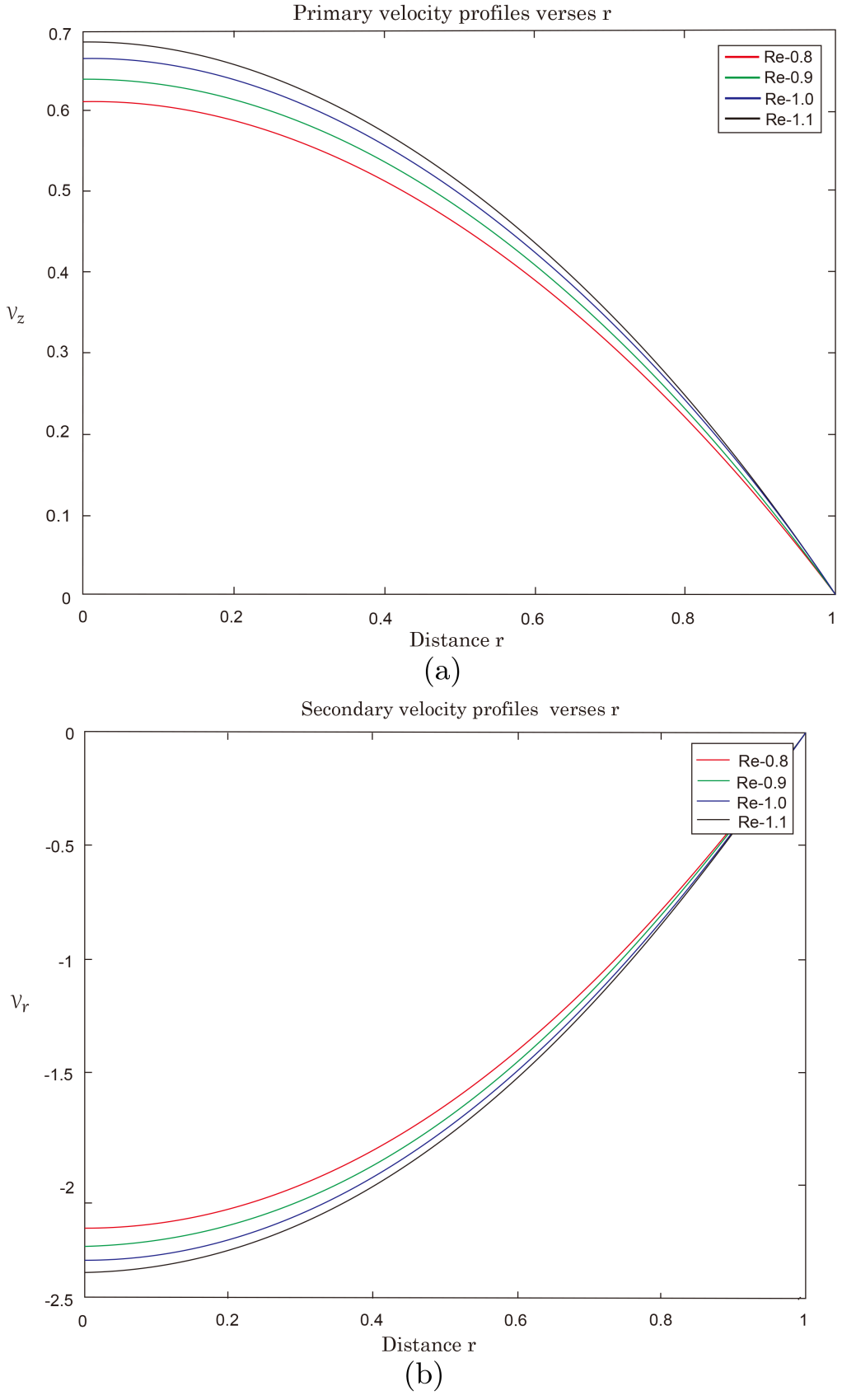

Figure 2. Graph of effects of Reynolds number on primary and secondary velocity profiles.

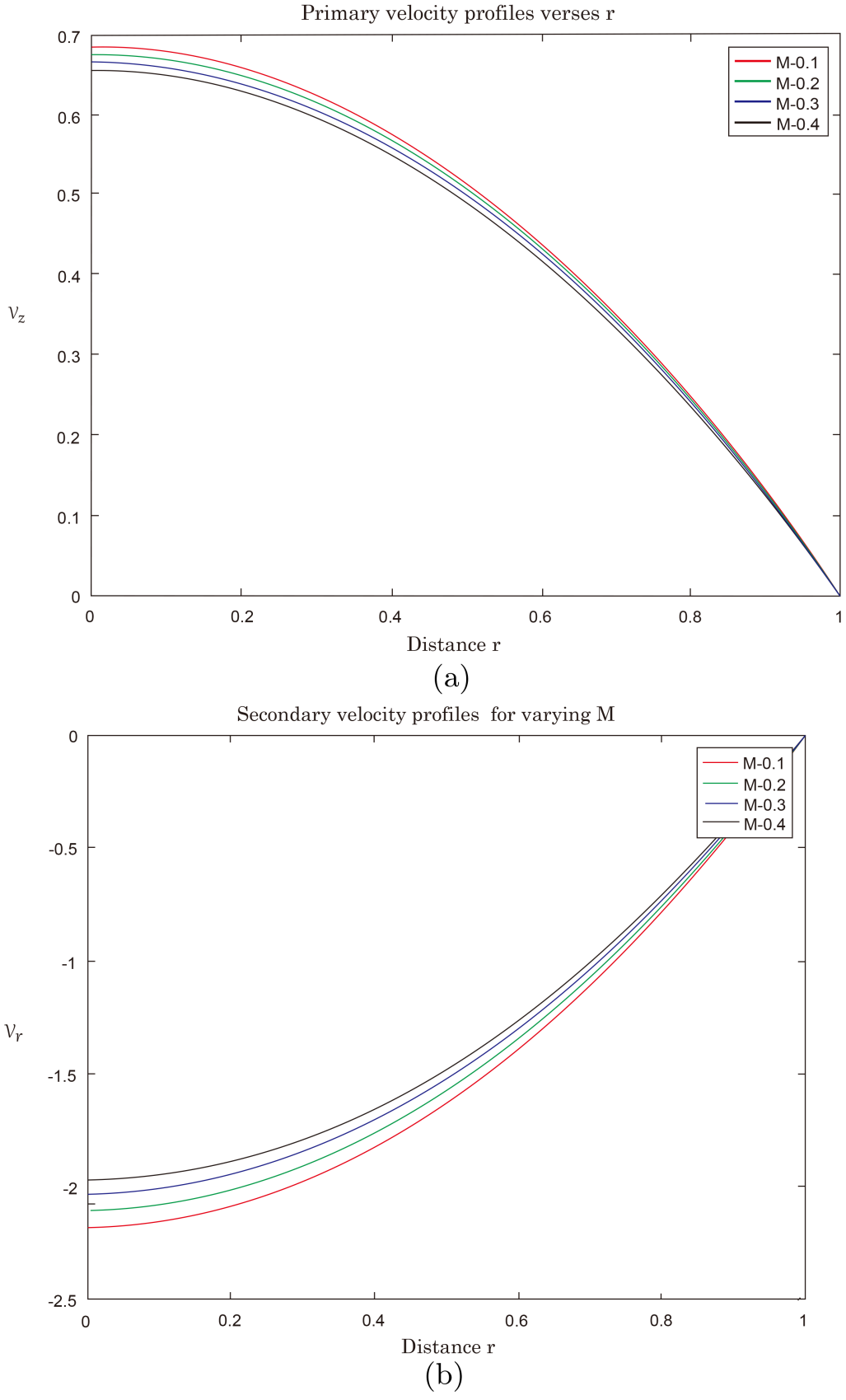

Figure 3. Graph of effects of Hartman number on primary and secondary velocity profiles.

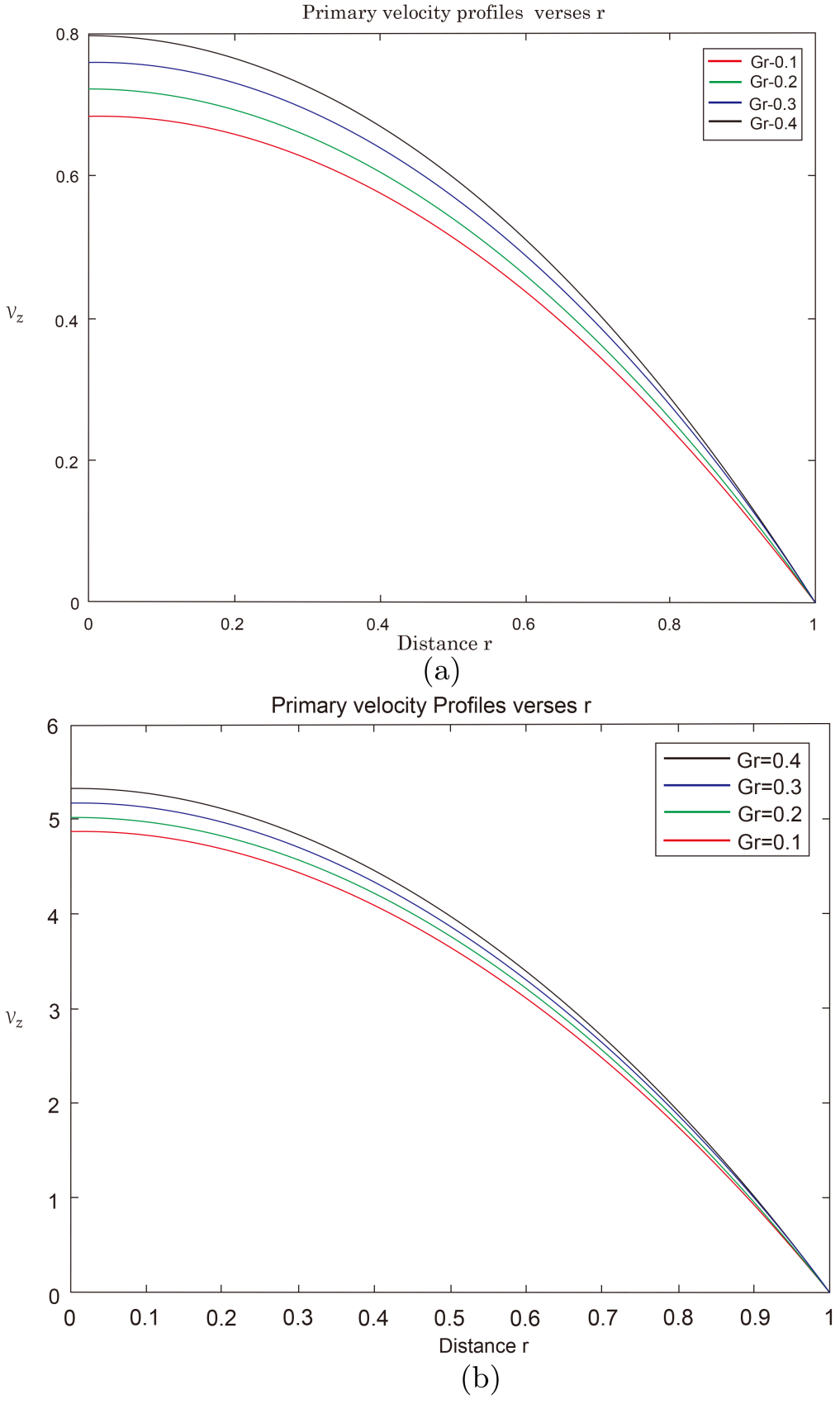

Figure 4. Graph of effects of Grashof number on primary velocity profiles.

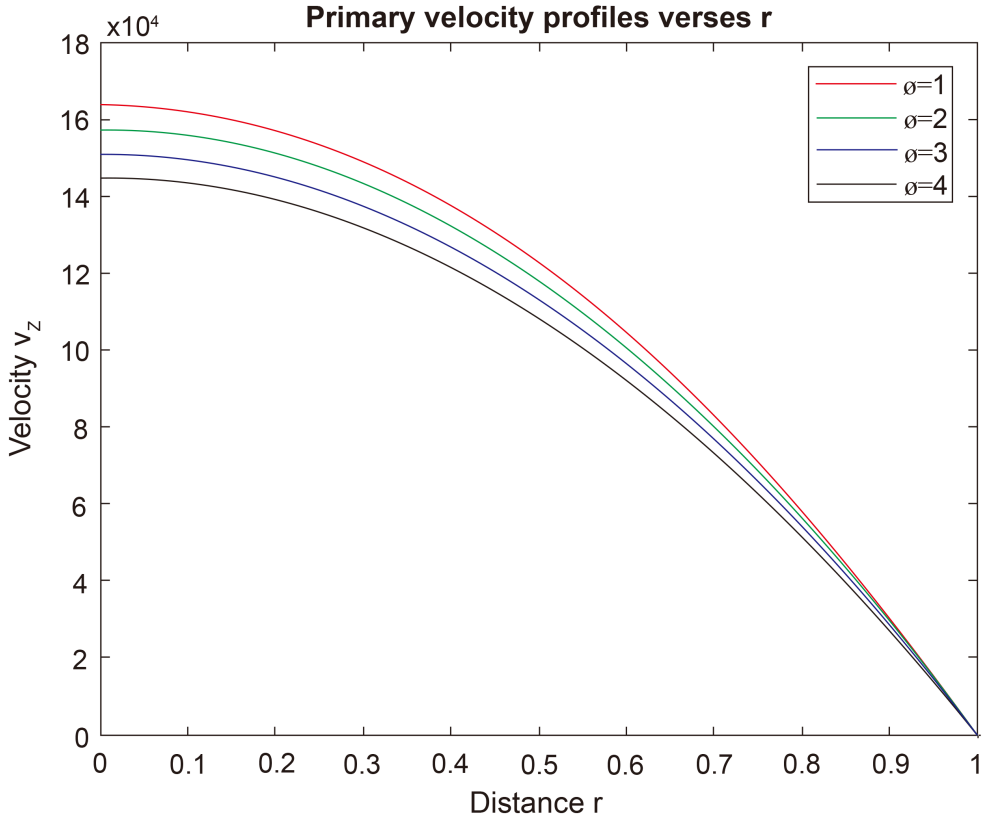

Figure 5. Graph of Effects of nanoparticle volume fraction on primary velocity profiles.

due to the free convection currents driven by the temperature differences in the fluid as well as the enhanced thermal buoyancy force. **Figure 4(b)** is observed that velocity profiles increases as concentration Grashof number is increased. Increase in primary velocity profiles is attributed to enhanced buoyancy forces which accelerate the fluid leading to increases velocity profiles. Grashof number has no effect on the secondary velocity profiles since the flow in radial direction in the fluidized bed dryer is primarily driven by pressure gradient and not buoyancy forces.

Figure 5 shows that fluid velocity decreases with increase in nanoparticle volume fraction. As nanoparticles volume fraction is increased, the fluid viscosity also increases. This increased viscosity results in greater flow resistance within the fluid flow resulting in the decrease in velocity profiles. The combination of increase in fluid velocity and improved thermal conductivity due to addition of silver nanoparticles contribute to the enhancement in the overall rate of heat transfer.

4.2. Temperature Profiles

In **Figure 6**, it is observed that an increase in Reynold number leads to increase in temperature. As Reynolds number increases, inertial forces dominate which signifies increased fluidization within the dryer. Increased fluidization leads to an increase in convective heat transfer within the fluid flow. This results in

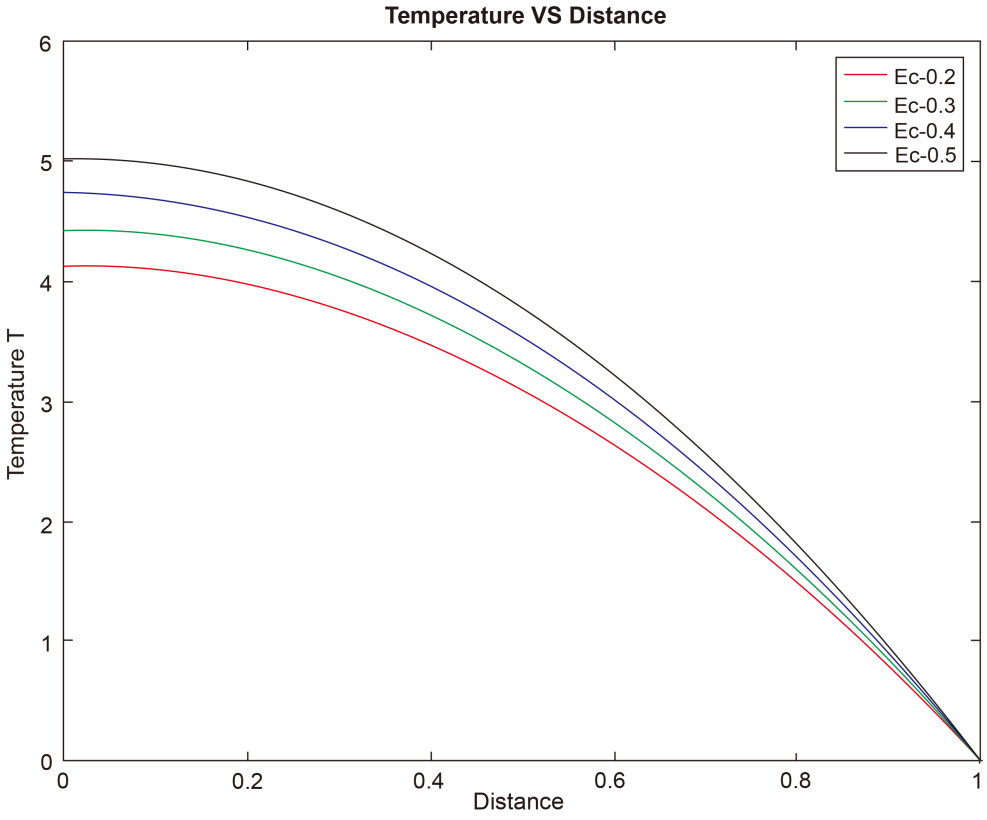

Figure 6. Graph of effects of Reynolds number on temperature profiles.

improved heat transfer between the fluid and the particles in the dryer. Thus, high Reynolds number increases heat transfer rate hence more efficient exchange of thermal energy within the dryer.

The temperature of the fluid rises as Eckert number (Ec) increases as presented in **Figure 7**. Eckert number gives the relationship of kinetic energy and thermal energy in the flow. The Ec number quantifies conversion of kinetic energy into internal energy, through the work done against viscous fluid stresses which resist motion of the fluid and cause energy dissipation. The additional energy released from viscous forces leads to increase in fluid's kinetic energy, which is depicted by the increase in temperature profiles.

Figure 8 reveals that temperature increases with increase in nanoparticle volume fraction ϕ. Increasing the volume of the silver nanoparticles leads to an overall increase in thermal conductivity of the nanofluid. This can be explained from the fact that zinc has a high thermal conductivity. Furthermore, nanoparticles are small in size thus have large surface area compared to their volume. Having large surface area allows nanoparticles interact more with the fluid in the dryer which allows for more efficient heat transfer between the fluid and tea particles. As volume of nanoparticles increases, convective heat transfer is improved which results in the rise of the fluid's temperature. Therefore, increase in thermal conductivity leads to more efficient heat transfer within the fluid.

Increase of radiation parameter leads to an increase in temperature as observed

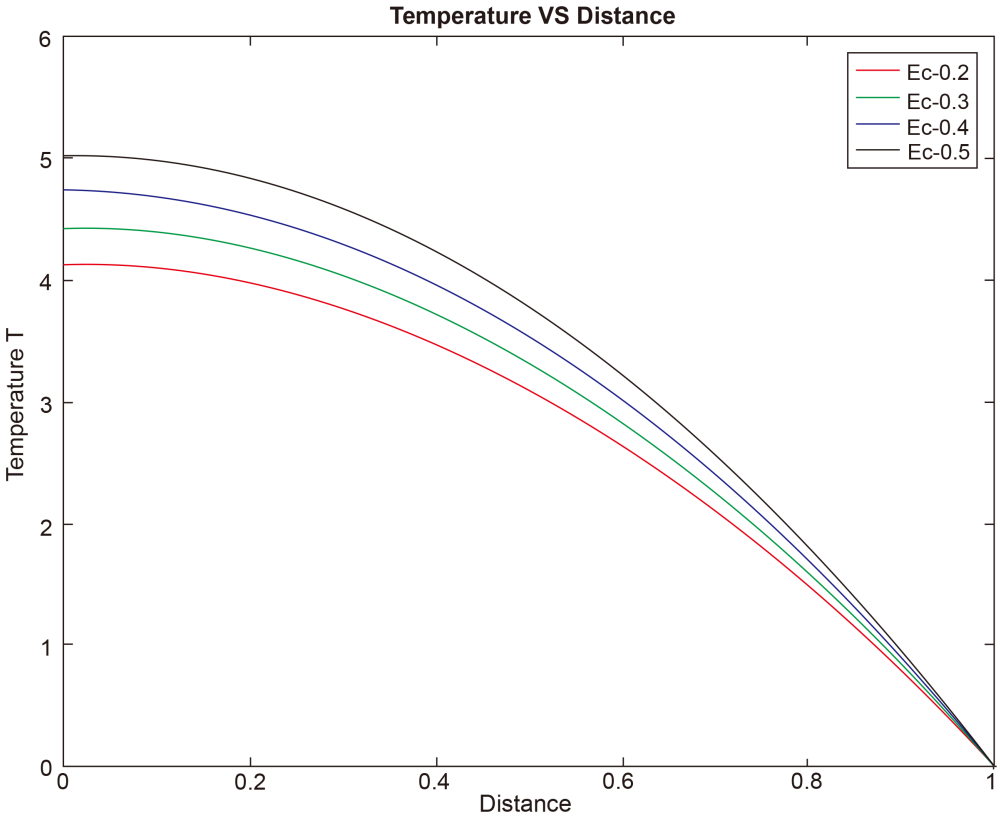

Figure 7. Graph of effects of Eckert number on temperature profiles.

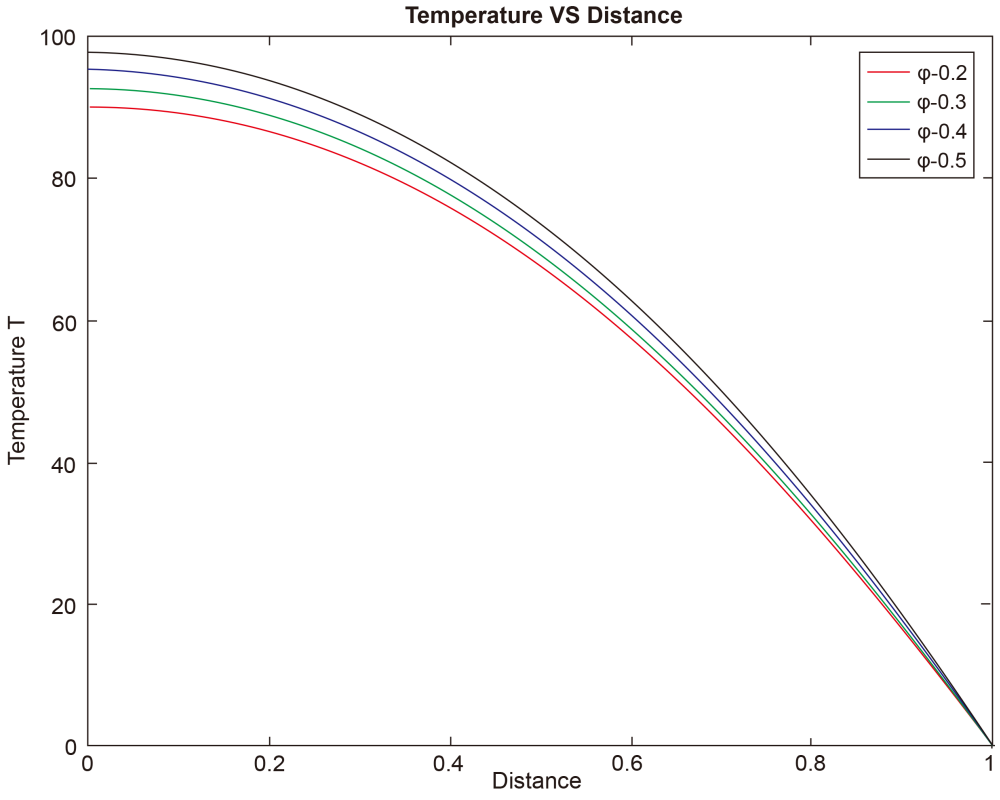

Figure 8. Graph of effects of nanoparticle volume fraction on temperature profiles.

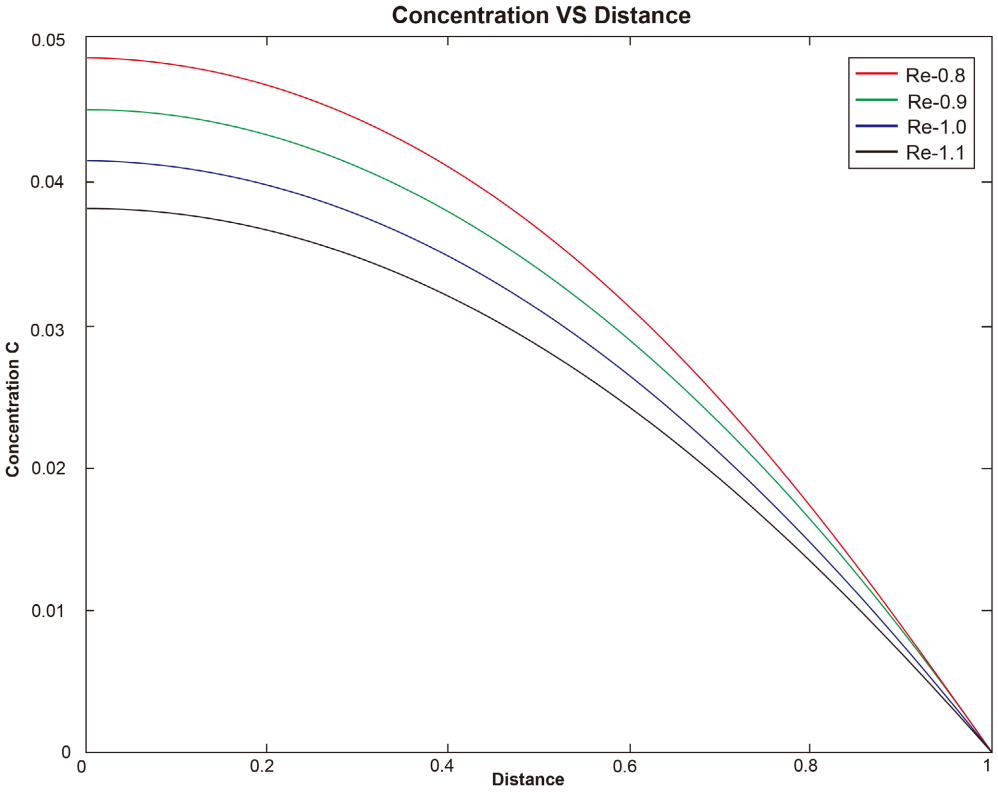

Figure 9. Graph of effects of radiation parameter on temperature profiles.

in **Figure 9**. This signifies the effectiveness of thermal radiation as a form of heat transfer in the dryer compared to other forms of heat transfer. Increase in radiation parameter consequently decreases the thermal boundary layer thickness. This results in heat being transferred in a more efficient manner hence increase in radiation parameter leading to increased temperature profiles.

4.3. Concentration Profiles

Increase in Reynolds number leads to a decrease in concentration profiles as observed in **Figure 10**. This can be explained in terms of balance between viscous and inertial forces. Increase in Re implies inertial forces are dominant compared to viscous forces in the flow resulting in raise of fluid velocity. The increase in fluid velocity leads to reduction of species from the surface of the dryer thus reducing species concentration.

Schmidt number gives the ratio of momentum to mass diffusivity and provides a measure of effectiveness of mass transport by diffusion in concentration boundary layer. In **Figure 11**, it is observed that increase in Sc number leads to a reduction in concentration profiles. When Sc is high, momentum diffuses quickly than mass which results in more uniform species distribution hence reducing the concentration profiles.

As shown in **Figure 12**, increasing the chemical reaction parameter results in increase of the fluid concentration. This can be attributed to the increase in the thickness of the concentration boundary layer, which consequently increases the

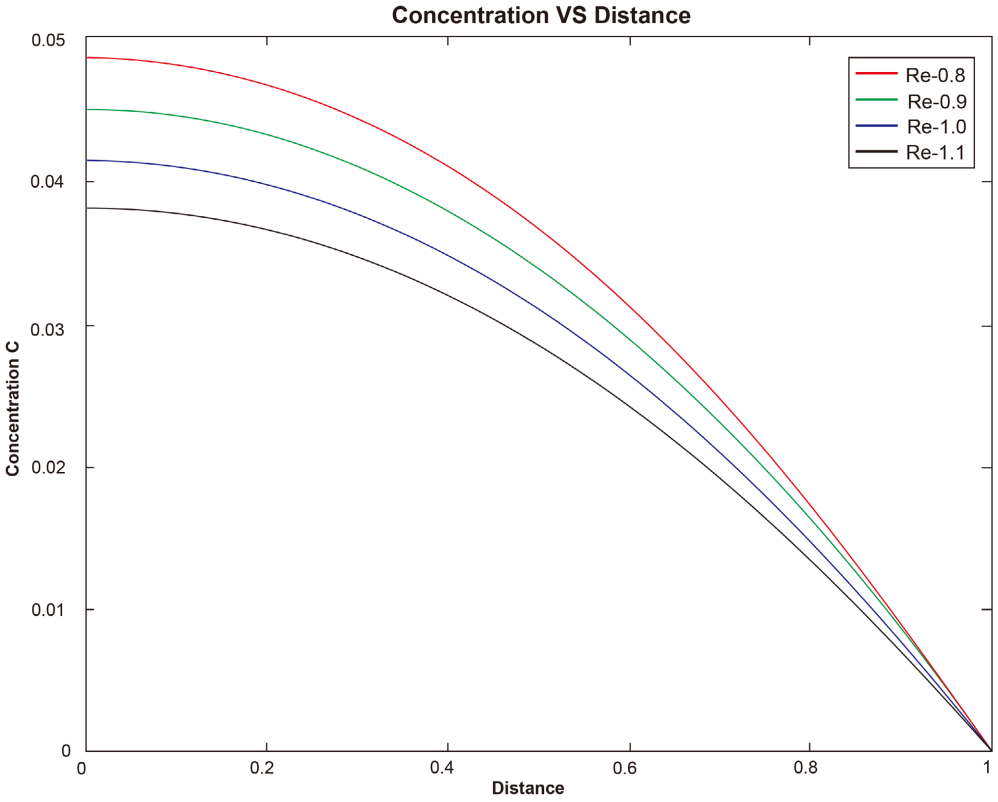

Figure 10. Graph of effects of Reynolds number on concentration profiles.

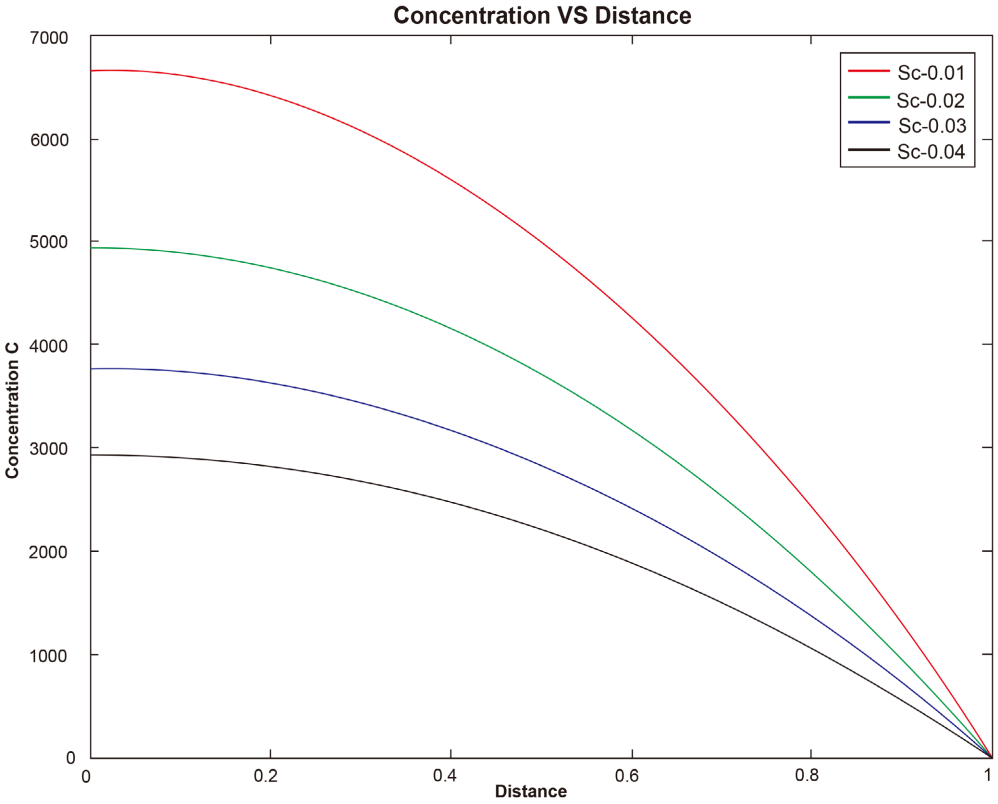

Figure 11. Graph of effects of Schmidt number on concentration profiles.

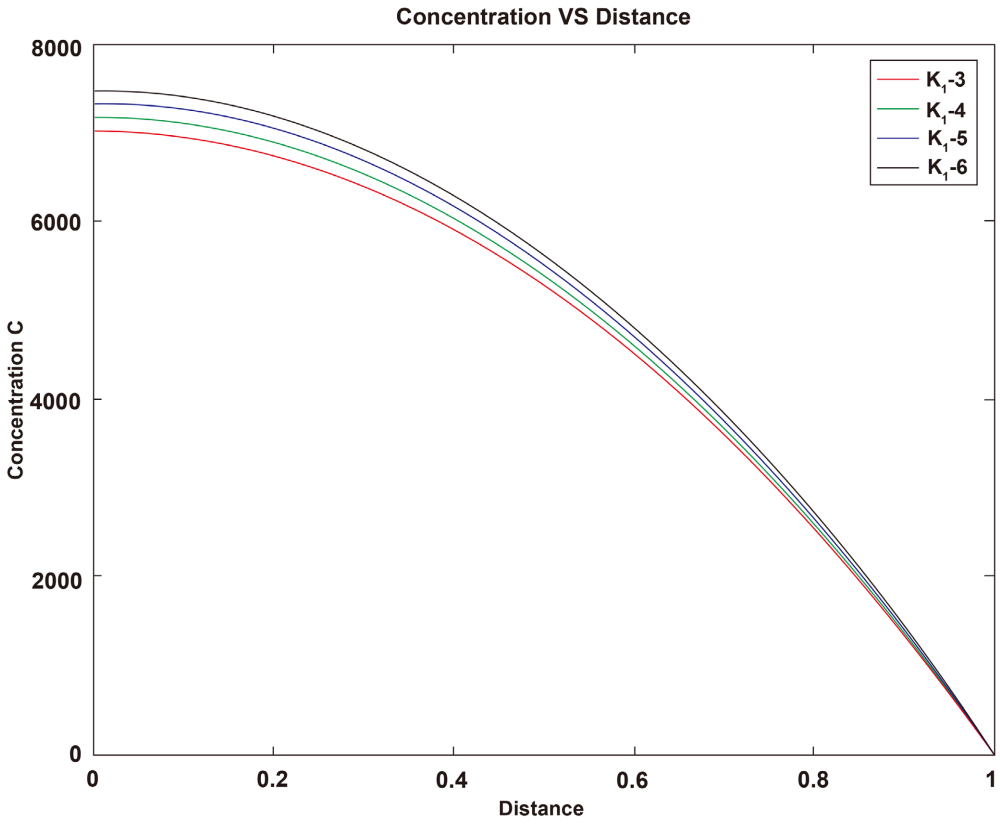

Figure 12. Graph of effects of chemical reaction parameter on concentration profiles.

concentration of the fluid.

4.4. Magnetic Induction Profiles

In Figure 13, it is observed that increase in Reynold number leads to high induced magnetic field. Re is the ratio of inertial to viscous forces and as it increases, influence of viscous forces reduces thus allowing more interaction of the fluid with the magnetic field. This consequently results in increased induced magnetic field.

Figure 14 shows that rise in magnetic Prandtl number leads to an increase in induced magnetic field. Magnetic Prandtl number gives a comparison of the strength of magnetic diffusivity to kinematic viscosity. High Magnetic Prandtl number shows that magnetic diffusivity is dominant over kinematic viscosity and the fluid has greater ability to diffuse magnetic fields when compared to its ability to dissipate kinetic energy. This then leads to the increase of induced magnetic field with rise of magnetic Prandtl number.

5. Validation

The results obtained in this study are validated by making a comparison between the computed results and those obtained by [16]. Based on their findings, they noted that the mean air velocity was minimum on the bed of the dryer's wall and highest at the center of the dryer. Furthermore, [6]'s study agrees with our findings

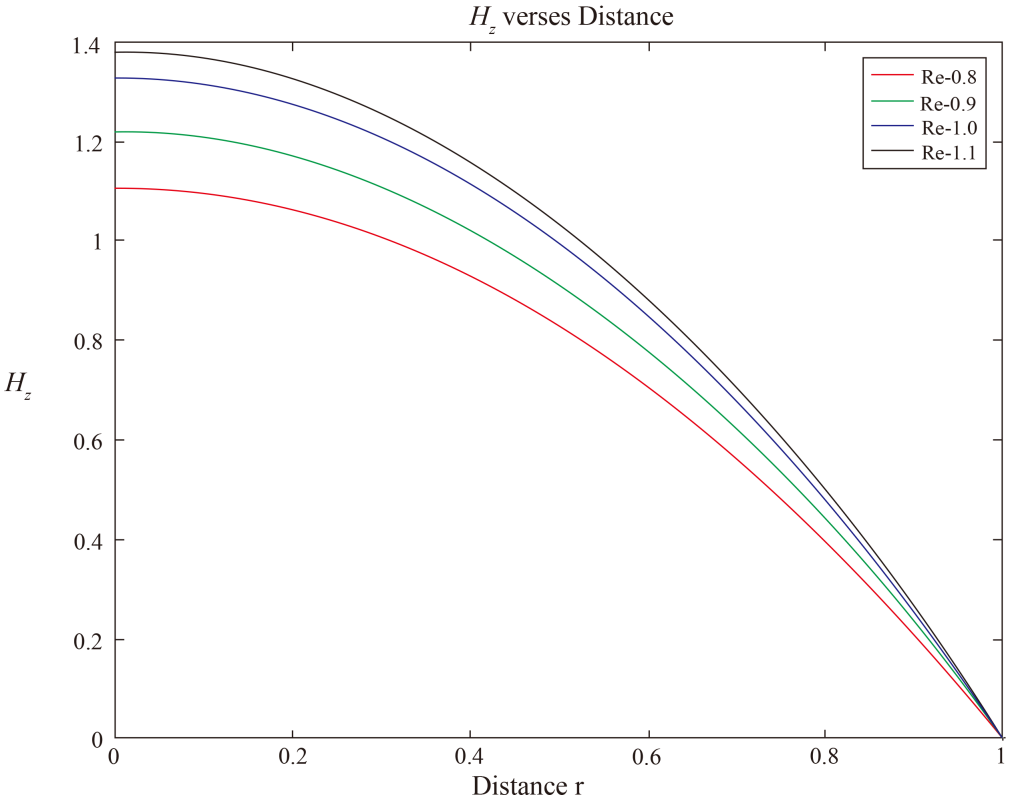

Figure 13. Graph of effects of Reynolds number on induced magnetic profiles.

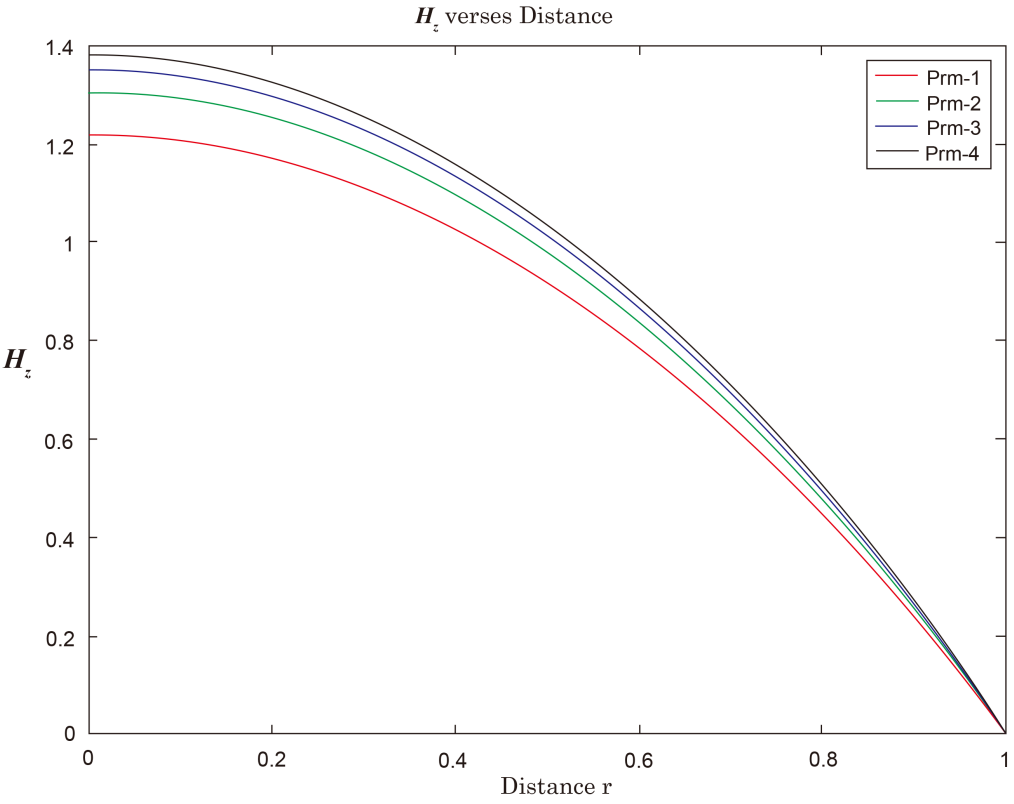

Figure 14. Induced magnetic profiles for varying magnetic Prandtl number.

that drying process in fluidized bed dryer is influenced by the coupled heat and mass transfer processes occurring in a fluidized bed dryer between fluid and solid particles and this process can be significantly improved by increasing dryer's temperature and inlet gas velocity.

6. Conclusions

In this article, unsteady hydromagnetic nanofluid flow within a fluidized bed dryer used in tea processing industries is studied. The problem is modeled by use of non-linear differential equations in presence of magnetic and buoyancy forces. The differential equations are non-dimensionalized and then solved using the Finite Difference Method. The numerical simulations done using MATLAB led to the following conclusions:

- Increasing Reynold number and Grashof number for heat and mass transfer led to enhanced primary velocity profiles. Moreover, increasing the nanoparticle volume fraction enhances the fluid flow. However, increase in Hartmann number decreases the fluid flow.
- The increase in Eckert number, Reynold number, and radiation parameter and nanoparticle fraction led to the corresponding rise in temperature within the dryer.
- Fluid velocity is not influenced by Grashof and Eckert numbers.
- Concentration profiles exhibited a decrease within the dryer with increase in Reynolds number, Schmidt number and chemical reaction parameter.
- Increase in magnetic Prandtl number and Reynolds number led to an increased induced magnetic field.

From our research findings, optimizing the performance of fluidized bed dryer in tea drying can be achieved by incorporating innovative techniques such as addition of nanoparticles and introduction of magnetic fields. These techniques can offer practical insights for tea processing industries seeking faster drying rates, reduced energy use and high-quality production.

Acknowledgments

The authors are grateful to the African Union Commission and the Pan African University, Institute for Basic Sciences, Technology and Innovation for their unwavering support in this research.

Conflicts of Interest

The authors declare no conflicts of interest regarding the publication of this paper.

References

[1] Onduru, D.D., De Jager, A., Hiller, S. and Van den Bosch, R. (2012) Sustainability of Smallholder Tea Production in Developing Countries: Learning Experiences from Farmer Field Schools in Kenya. *International Journal of Development and Sustainability*, **1**, 714-742.

[2] Alvarez, P. and Shene, C. (1996) Experimental Study of the Heat and Mass Transfer during Drying in a Fluidized Bed Dryer. *Drying Technology*, **14**, 701-718. https://doi.org/10.1080/07373939608917121

[3] Villegas, J.A., Li, M., Duncan, S.R., Wang, H.G. and Yang, W.Q. (2008) Modeling and Control of Moisture Content in a Batch Fluidized Bed Dryer Using Tomographic Sensor. *2008 American Control Conference*, Seattle, WA, 11-13 June 2008, 3350-3355. https://doi.org/10.1109/ACC.2008.4587009

[4] Wang, Z.H. and Chen, G.H. (2000) Heat and Mass Transfer in Batch Fluidized-Bed Drying of Porous Particles. *Chemical Engineering Science*, **55**, 1857-1869. https://doi.org/10.1016/S0009-2509(99)00446-7

[5] Sae-Heng, S., Swasdisevi, T. and Amornkitbamrung, M. (2011) Investigation of Temperature Distribution and Heat Transfer in Fluidized Bed Using a Combined CFD-DEM Model. *Drying Technology*, **29**, 697-708. https://doi.org/10.1080/07373937.2010.528107

[6] Wang, W., Wang, L.Y., Pan, Y.Q., Chen, M. and Chen, G.H. (2012) Two-Dimensional Mathematical Modeling of Heat and Mass Transfer in Fluidized-Bed Drying of Porous Material. *International Journal of Food Engineering*, **8**. https://doi.org/10.1515/1556-3758.2663

[7] Poós, T. and Szabó, V. (2017) Application of Mathematical Models Using Volumetric Transfer Coefficients in Fluidized Bed Dryers. *Energy Procedia*, **112**, 374-381. https://doi.org/10.1016/j.egypro.2017.03.1079

[8] Ozturk, M. and Dincer, I. (2019) Exergy Analysis of Tea Drying in a Continuous Vibro-Fluidised Bed Dryer. *International Journal of Exergy*, **30**, 376-391. https://doi.org/10.1504/IJEX.2019.104102

[9] Valiallah Mousavi, S., Sheikholeslami, M., Barzegar Gerdroodbary, M., *et al.* (2016) The Influence of Magnetic Field on Heat Transfer of Magnetic Nanofluid in a Sinusoidal Double Pipe Heat Exchanger. *Chemical Engineering Research and Design*, **113**, 112-124. https://doi.org/10.1016/j.cherd.2016.07.009

[10] Sheikhzadeh, G., Ghasemi, H. and Abbaszadeh, M. (2016) Investigation of Natural Convection Boundary Layer Heat and Mass Transfer of MHD Water-Al_2O_3 Nanofluid in a Porous Medium. *International Journal of Nano Studies & Technology* (*IJNST*), **5**, 110-122. https://doi.org/10.19070/2167-8685-1600021

[11] Aminian, E., Moghadasi, H. and Saffari, H. (2020) Magnetic Field Effects on Forced Convection Flow of a Hybrid Nanofluid in a Cylinder Filled with Porous Media: A Numerical Study. *Journal of Thermal Analysis and Calorimetry*, **141**, 2019-2031. https://doi.org/10.1007/s10973-020-09257-y

[12] Davidson, P.A. (2001) An Introduction to Magnetohydrodynamics. Cambridge University Press, Cambridge. https://doi.org/10.1017/CBO9780511626333

[13] Riaz Khan, M., Li, M.X., Mao, S.P., Ali, R. and Khan, S. (2021) Comparative Study on Heat Transfer and Friction Drag in the Flow of Various Hybrid Nanofluids Effected by Aligned Magnetic Field and Nonlinear Radiation. *Scientific Reports*, **11**, Article No. 3691. https://doi.org/10.1038/s41598-021-81581-1

[14] Hayat, T., Ahmed, B., Abbasi, F.M. and Alsaedi, A. (2017) Hydromagnetic Peristalsis of Water Based Nanofluids with Temperature Dependent Viscosity: A Comparative Study. *Journal of Molecular Liquids*, **234**, 324-329.

[15] Tinega, A.K. and Ndede, C.O. (2018) Stability and Consistency Analysis for Central Difference Scheme for Advection Diffusion Partial Differential Equation. *International Journal of Science and Research* (*IJSR*), **7**, 1046-1049.

[16] Keshavarz Moraveji, M., Kazemi, S.A. and Davarnejad, R. (2011) CFD Modeling of Heat and Mass Transfer in the Fluidized Bed Dryer. *Trends in Applied Sciences Research*, **6**, 595-605. https://doi.org/10.3923/tasr.2011.595.605

Nomenclature

(v_r, v_z) —Velocity components ($m \cdot s^{-1}$)
T_∞ —Free stream temperature (K)
T_b —Temperature at the dryer's bed (K)
C_b —Concentration at the dryer's bed ($Mol \cdot m^{-3}$)
B_0 —Applied magnetic field ($Wb \cdot m^{-2}$)
P—Pressure ($N \cdot m^{-2}$)
F_b —Buoyancy force (N)
g—Acceleration due to gravity ($m \cdot s^{-2}$)
k_s —Solid fraction thermal conductivity (W/m.K)
k_{nf} —Nanofluid thermal conductivity (W/m.K)
$\mu_n f$ —Dynamic viscosity of nanofluid ($kg \cdot m^{-1} \cdot s^{-1}$)
$\rho_n f$ —Nanofluid density (kg^{-3})
D_{nf} —Diffusion coefficient ($m^2 \cdot s^{-1}$)
$(\rho C_p)_{nf}$ —Nanofluid heat capacitance (J/K)
g_z —gravitational force along z direction ($m \cdot s^{-2}$)
F_{EM} —Lorentz force (N)
σ_{nf} —Electrical conductivity ($\omega^{-1} \cdot m^{-1}$)
Q^* —Heat source (J)
k_r —Chemical reaction parameter
U, V —Dimensionless velocity
Re —Reynolds number
Gr_T —Thermal Grashof number
Gr_C —Concentration Grashof number
M—Hartmann number
Pr —Prandtl number
Pr_m —Magnetic Prandtl number
Sc —Schmidt number